Thin–Walled Structures 159 (2021) 107245

Contents lists available at ScienceDirect

Thin-Walled Structures

journal homepage: http://www.elsevier.com/locate/tws

Towards the prediction of hydrogen–induced crack growth in high–graded strength steels

B. Sobhaniaragh *, S.H. Afzalimir, C. Ruggieri

Fracture Mechanics and Structural Integrity Research Group (NAMEF), Department of Naval Architecture and Ocean Engineering, Polytechnic School, University of São Paulo (USP), Brazil

ARTICLE INFO

Keywords:
Hydrogen embrittlement
Ductile crack growth
Cohesive–interface elements
Park–paulino–roesler (PPR) model
Hydrogen enhanced localized plasticity
Crack growth resistance curve

ABSTRACT

This work addresses a hydrogen–induced cracking methodology incorporating the fully coupled problems of elastoplastic deformation and hydrogen transport within cohesive–interface elements framework to predict ductile tearing in high strength steels. In the present work, on one hand, the flow stress declines with escalating hydrogen concentration and, as a result, taking into account the hydrogen impact on enhancing plastic deformation in the lattice through the hydrogen enhanced localized plasticity (HELP) model. On the other hand, to implement hydrogen impact into the cohesive–interface elements in the hydrogen enhanced decohesion (HEDE) manner, a phenomenological decohesion model is adopted, leading to combining the both mechanisms (HELP + HEDE). Furthermore, a nonlinear traction–separation relationship based on the Park–Paulino–Roesler (PPR) model determines the constitutive response of the zero thickness cohesive–interface elements while the finite–strain, incremental plasticity model is accounted for the bulk material. The hydrogen–degraded PPR model provides a flexibility and control over various softening behaviours, from a convex brittle to a concave ductile shape. This computational framework is established to simulate ductile crack extension in a C(T) specimen made of AISI 4130 high strength steels. Afterwards, the parameters involved in the hydrogen–degraded PPR model are properly calibrated with experimental data for the uncharged and hydrogen–charged C(T) specimens. The key contributions of this study are to shed light on the hydrogen concentration (lattice and trapped) effects on the crack growth resistance curves and stress triaxiality. Based on the results obtained for AISI 4130 high strength steels, it has been concluded that the lattice hydrogen has the dominating factor in the hydrogen degradation compared with trapped hydrogen.

1. Introduction

The escalating demand for energy and clean resources has triggered two main developments. *On one hand*, it has spurred a flurry of exploration and production activities of oil and natural gas in more hostile environments, including very deep water offshore hydrocarbon reservoirs. One of the key challenges facing the oil and gas industry is the assurance of more reliable and fail–safe operations of the infrastructure for production and transportation. Currently, structural integrity of submarine risers and flow lines represents a key factor in operational safety of subsea pipelines. Advances in existing technologies favor the use of cathodic protection in C–Mn steel pipelines as an effective technology to prevent metal corrosion in marine and aggressive environments [1]. However, the electrochemical reactions associated with the cathodic protection system have strong potential to produce atomic hydrogen at the metal surface which can diffuse and enter into the crystalline steel structure causing hydrogen–induced degradation of mechanical and toughness properties, often termed hydrogen embrittlement (HE) [2,3]. *On the other hand*, the mitigation of greenhouse gas emissions has triggered opening a new research field towards the use of hydrogen as an energy carrier for the future energy demands. Nonetheless, progress towards a hydrogen–based economy would demand to set up substructure so as to produce, transport and store hydrogen. Among other probabilities, the use of existing widespread pipeline networks appears to be among the most reliable solutions for hydrogen transport [4]. Notwithstanding, the presence of hydrogen in steel pipelines might cause the pipeline to become more susceptible to HE.

HE is one of the most complicated phenomena of degradation in metallic materials, signifying a hydrogen–induced transition from a high–toughness ductile fracture (micro–void coalescence) to a

* Corresponding author.
E-mail address: behnam@usp.br (B. Sobhaniaragh).

https://doi.org/10.1016/j.tws.2020.107245
Received 23 May 2020; Received in revised form 10 September 2020; Accepted 27 October 2020
Available online 24 November 2020

brittle–type of fracture (either by a transgranular or intergranular mechanism). Indeed, HE manifests as loss in structural integrity of a vast range of metals and alloys, which may result in unexpected and premature catastrophic failures. To date, the definite mechanisms underlying HE are still under debate; at least two crucial mechanisms have been proposed [5]. The hydrogen enhanced decohesion (HEDE) mechanism assumes interstitial atomic hydrogen reduces the cohesive strength of the lattice and, as a result, enhancing decohesion. According to the hydrogen enhanced localized plasticity (HELP) model, the presence of solute hydrogen enhances the mobility of dislocations leading to enhancing localized plastic deformation at the crack tip. Either model is promoted by a myriad of atomistic observations [6,7] and experimental data [8,9] and is contemplated as the underlying factor in particular fracture scenarios. A comprehensive micro–mechanical model of fracture carried out by Novak et al. [10], which accounted for the effect of atomic hydrogen on HE of high–strength steels, reported the synergistic interplay of both HELP and HEDE. Furthermore, it has been shown that the coupling mechanisms of HELP and HEDE not only advocate intergranular, ductile behavior, and micro–void coalescence modes of fracture in steels, but did it also influence quasi–cleavage fracture. In the numerical simulation, some works adopted only one of the dominating HE mechanisms. For instance, taking the HELP model into account, a hydrogen affected plasticity model has been implemented [11–13] while as far as the simulation in the HEDE manner is concerned, a phenomenological decohesion model was established [14–24]. Notwithstanding, in the present work, both predominant HE mechanisms (HEDE + HELP) are considered, which will be discussed more in the next parts.

The numerical simulation of hydrogen–induced fracture [11–34], as a multi–physics approach, which couples hydrogen transport, plastic deformation, fracture and their interactions, has gained a substantial attention. A phase field formulation for hydrogen–assisted cracking in the framework of the finite element method (FEM) has been presented by Martínez-Pañeda et al. [26]. Furthermore, a phase field regularized cohesive zone model (PF–CZM) for hydrogen–induced cracking was introduced by Wu et al. [14]. They introduced two distinct HEDE models by incorporating several implicitly defined hydrogen–dependent softening laws. However, HELP mechanism has not been taken into account. Ahn et al. [11] conjectured that the material softening takes place owing to the presence of hydrogen, which affects the void process ahead of the crack tip. They employed a unit cell containing a single void and used the results to adjust the traction separation law (TSL). Using similar methodology, the effects of hydrogen–induced material softening and lattice dilatation on void growth have been investigated by Liang et al. [12]. Olden et al. [15,27,28] investigated a three–step FE procedure including elastic–plastic stress analysis, hydrogen diffusion analysis and hydrogen–informed CZM analysis for HE simulation. To include the hydrogen influence in the HEDE manner into the analysis, the hydrogen degradation law proposed by Serebrinsky et al. [35] was established. De Meo et al. [30] modeled adsorbed–hydrogen stress–corrosion cracking of a polycrystalline AISI 4340 high–strength low–alloy steel plate using a multiphysics peridynamic framework. A two–step analysis has been introduced by Díaz et al. [22] for the HE problem; first hydrogen distribution was obtained with diffusion equations modified by the stress–strain state and afterwards, a CZM was included to model damage initiation. Moreover, the fully coupled and weekly coupled FE–CZM adopting the thermal–stress analysis and the analogy between hydrogen diffusion and heat transfer have been presented by Gobbi et al. [20,34]. Furthermore, Jemblie [24] simulated hydrogen–induced fracture initiation in a hot rolled bonded clad steel pipe using the CZM with a polynomial TSL. The same authors [36] carried out a comprehensive review on the CZM for numerically assessing HE of steel structures.

Taking CZM–based hydrogen–induced cracking into account, the constitutive behavior of cohesive–interface elements is described by the so–called TSL, which is usually characterized by the critical cohesive strength and the cohesive energy (or critical separation). Various failure scenarios and factors influencing the failure behavior can be dealt with by manipulating the TSL. In the HE modelling, serval types of TSL have been employed including the bilinear TSL [18], the trapezoidal TSL [16,17,20,34], the exponential TSL [37], and the polynomial TSL [15,19,23,24,27,28,38]. However, in the present work, a unified potential–based CZM, the Park–Paulino–Roesler (PPR) model [39] is employed for the hydrogen degradation TSL, which addresses the drawbacks of the prevailing either nonpotential–based or potential–based CZM in the literature, in particular with respect to mode–mixity, user flexibility, and consistency [40,41]. Most importantly, it provides for several material failure behaviors by permitting the modeler to determine the shape of the softening curve in both normal and shear traction–separation relations whereas in most TSL, softening behavior is hard–coded and cannot be modified. This aspect is highlighted in the CZM–based hydrogen degradation. It is because using the PPR model in the degradation process provides a control over various softening behaviours, from a convex brittle to a concave ductile shape. This capability is also substantially applicable in the calibration of the cohesive parameters used in numerical modelling with experimental data.

There are still controversial opinions in the literature regarding the impact of hydrogen trapping at microstructural defects upon HE. It is debatable whether trapped hydrogen (for instance at dislocations and at carbide particles) holds a critical role promoting hydrogen–induced fracture or hydrogen resided at normal interstitial lattice sites (NILS) plays a crucial role in HE [42]. Li et al. [43] conjectured that trapping sites such as austenite grain boundaries, martensite interfaces, and dislocation retaining a robust affinity to hydrogen can avoid hydrogen from segregating to crack tip and alleviate HE. Furthermore, Yamasaki and Bhadeshia [44] concurred with this view and studied the peak trapping affinity of carbides to hydrogen in martensitic steels so as to alleviate the detrimental impacts of hydrogen upon mechanical performance. Moreover, Ayas et al. [45] concluded that the presence of lattice hydrogen escalates the susceptibility to HE whilst trapped hydrogen has only a negligible influence. On the contrary, Novak et al. [10] claimed that hydrogen trapped at the dislocations is the underlying factor of HE in high strength steels. In agreement with this finding, calculations conducted by Dadfarina et al. [13] did not support the argument that strong or irreversible traps in a material is a way to mitigate HE.

The main objective of the present work is to present a CZM–based hydrogen–induced cracking methodology incorporating the fully coupled problems of elastoplastic deformation and hydrogen transport to predict ductile tearing in high strength steels. A nonlinear traction–separation relationship based on the PPR model determines the constitutive response of the zero thickness cohesive–interface elements while the finite–strain, incremental plasticity model is accounted for the bulk material. The hydrogen–degraded PPR model, which has four physical fracture parameters, enables flexibility in the softening shape in TSL. In this work, the flow stress declines with escalating hydrogen concentration and, as a result, considering the hydrogen impact on promoting plastic deformation in the lattice in the HELP manner. In addition, to implement hydrogen influence into the cohesive–interface elements through the HEDE principle, the hydrogen degradation law introduced by Serebrinsky et al. [35] is adopted, leading to combining the both mechanisms of HEDE + HELP. This computational framework is employed to simulate ductile crack extension in a C(T) specimen made of AISI 4130 high strength steel. The involved parameters in the PPR model are satisfactorily calibrated with the uncharged and hydrogen–charged specimens data. Then, the influence of hydrogen concentration (NILS and trapped) on the hydrogen coverage profile ahead of the crack tip is investigated in detail. Furthermore, the crack growth resistance curves for the uncharged and hydrogen–charged C(T) specimens are discussed. Last but not least, the distribution of stress triaxiality ahead of crack tip as a function of the NILS hydrogen contents and hydrogen–induced softening is assessed.

2. Hydrogen transport model in a deforming material

The process that results in HE includes a transport stage of hydrogen to the site of degradation. In order to predict the degrading effect of hydrogen on the mechanical properties, it is of fundamental importance to correctly assess the hydrogen distribution in the material. In this work, we assume that hydrogen atoms are generally considered to reside either at NILS or being trapped at microstructural heterogeneities such as dislocations, grain boundaries, precipitates, inclusions, voids, and interfaces. Traps normally lower the amount of mobile hydrogen, hence reducing the apparent diffusivity and raising the local solubility of the system. The hydrogen atoms in lattice and trap sites are assumed to be in equilibrium with the mean stress and equivalent plastic strain. Based on Oriani's equilibrium theory [46], the occupancy of the trapping sites, θ_T, with a corresponding trap binding energy is related to the NILS occupancy, θ_L, through

$$\frac{\theta_T}{1-\theta_T}=\frac{\theta_L}{1-\theta_L}K_T \tag{1}$$

where $K_T=\exp(\mathrm{W}_B/\mathrm{R}T)$ is the equilibrium constant, W_B is the trap binding energy, R is the universal gas constant, and T is the absolute temperature. The hydrogen concentration in NILS, C_L, measured in hydrogen atoms per unit volume, is expressed by $C_L=\beta\theta_L N_L$ where β designates the number of NILS per solvent atom, $N_L=N_A/V_M$ denotes the density of solvent atoms per unit lattice volume, N_A is Avogadro's number, and V_M, measured in unit of volume per mole, denotes the molar volume of the host metal. The concentration of hydrogen in the trapping sites is written as $C_T=\alpha\theta_T N_T$, where α denotes the number of sites per trap and N_T is the corresponding trap density which varies point–wise dependent on the local plastic strain level. In this work, the trap density model proposed by Sofronis et al. [47] is considered as follows

$$N_T=\sqrt{2}\rho\Big/\tilde{a} \tag{2}$$

where $\tilde{a}$ is the lattice parameter and ρ is the dislocation density (calculated in dislocation line length per cubic meter), which varies with the equivalent plastic strain such that [48].

$$\rho=\begin{cases}\rho_0+\gamma\varepsilon^p, & \varepsilon^p\le 0.5\\ \rho_0+0.5\gamma, & \varepsilon^p>0.5\end{cases} \tag{3}$$

where ρ_0 denotes the initial dislocation density for annealed material with $\varepsilon^p=0$, and $\gamma=2\times10^6$ line length/m^3 for body–centered cubic (bcc) iron.

Based on Fermi–Dirac statistics [49], NILS hydrogen concentration, C_L, is calculated with regard to initial NILS hydrogen concentration in the stress–free solid, C_L^{ini}, and the local hydrostatic stress, σ_{kk}, through

$$\frac{\theta_L}{1-\theta_L}=\frac{\theta_L^{ini}}{1-\theta_L^{ini}}K_L \tag{4}$$

where $\theta_L^{ini}=C_L^{ini}/\beta N_L$ is the initial NILS occupancy, and $K_L=\exp(\sigma_{kk}V_H/3\mathrm{R}T)$. Using Eqs. (1) and (4), one can obtain the total hydrogen concentration, $c=(C_L+C_T)/N_L$, measured in hydrogen atoms per solvent atom, as a function of initial NILS hydrogen concentration, C_L^{ini}, the effective plastic strain, ε^p, and the local hydrostatic stress as

$$c=\beta(\theta_L(\sigma_{kk})+\theta_{TL}(\sigma_{kk},\varepsilon^p)) \tag{5}$$

where

$$\theta_L(\sigma_{kk})=\frac{\theta_L^{ini}K_L(\sigma_{kk})}{((1-\theta_L^{ini})+\theta_L^{ini}K_L(\sigma_{kk}))} \tag{6}$$

and

$$\theta_{TL}(\sigma_{kk},\varepsilon^p)=\frac{\alpha}{\beta}\frac{N_T(\varepsilon^p)}{N_L}\frac{K_T\theta_L(\sigma_{kk})}{1-\theta_L(\sigma_{kk})+K_T\theta_L(\sigma_{kk})} \tag{7}$$

It should be noted that values of both the hydrostatic stress and the effective plastic strain depend on the corresponding amount of hydrogen concentration, which makes the derivation of hydrogen populations, plastic strains, and stresses fully coupled.

The underlying mechanism for the diffusion of hydrogen in steel is lattice diffusion as a result of interstitial jumps from one interstitial site to an adjacent one. The governing equation for transient hydrogen diffusion taking both hydrostatic drift and trapping into account is expressed by [50].

$$\frac{DV_H}{3\mathrm{R}T}C_L\sigma_{kk,i}+\alpha\theta_T\frac{dN_T}{d\varepsilon^p}\frac{d\varepsilon^p}{dt}+\frac{D}{D_{eff}}\frac{dC_L}{dt}-DC_{L,ii}=0 \tag{8}$$

in which ',' denotes a spatial derivative, d/dt is a time derivative, σ_{ij} is the Cauchy stress, D denotes the hydrogen diffusion coefficient through NILS, and D_{eff} is an effective diffusion coefficient defined by

$$\frac{D_{eff}}{D}=\left(1+\frac{\partial C_T}{\partial C_L}\right)^{-1} \tag{9}$$

By making use of Eqs. (1) and (2), Eq. (9) is expressed through

$$\frac{D_{eff}}{D}=\left(1+\frac{K_T\alpha\beta N_T N_L}{(\beta N_L+(K_T-1)C_L)^2}\right)^{-1} \tag{10}$$

It is worth noting that given the fast trap filling kinetics according to Oriani's model, the effective diffusion coefficient, D_{eff}, is less than NILS diffusion coefficient, D, while the traps are not saturated or as new traps are created due to plastic straining. All hydrogen related parameters are listed in Table 1.

3. Elastoplastic constitutive law

Birnbaum and Sofronis [51] introduced the HELP mechanism in which hydrogen atoms enhances the dislocation mobility in preferred crystallographic planes at the crack tip resulting in locally decreased shear strength. An experimental evidence of HELP was reported by Robertson [52]. Also, the results from the in–situ TEM deformation experiments in a hydrogen environment showed that the solute hydrogen can increase the velocity of dislocations and the crack propagation rate. From a continuum mechanics perspective, hydrogen–induced material softening can be explained by a local flow stress, σ_Y, which decreases with rising hydrogen concentration. Following Sofronis et al. [47], this correlation between the hydrogen effect and the local flow stress may be expressed by a phenomenological constitutive relation as

Table 1
Hydrogen related parameters for the model.

Properties	Symbol	Value
Number of NILS per host atom	B	6
Partial molar volume of hydrogen	V_H	2×10^{-6} m^3/mol
Variation of Gibbs free energy	ΔG_b^0	3×10^4 J/mol
Avogadro constant	N_A	6.023×10^{23} atoms per mole
Gas constant	R	8.31 J/mol.K
Dislocation density for annealed material ($\varepsilon^p=0$)	ρ_0	10^{10} m^{-2}
Coefficient for calculating dislocation density	Γ	2×10^{16} m^{-2}
Trap binding energy	W_B	21 kJ/mol
Number of trapping sites per dislocation	A	1
Molar volume of the host lattice	V_m	7.116×10^{-6} m^3/mol
Lattice parameter	$\tilde{a}$	2.86×10^{10} m

$$\sigma_Y(\varepsilon^p, c) = \sigma^{ini}(c)\left(1 + \frac{\varepsilon^p}{\varepsilon^{ini}}\right)^N \tag{11}$$

in which c is the total hydrogen concentration calculated in hydrogen atoms per solvent atom, $\sigma^{ini}(c)$ denotes the initial yield stress in the presence of hydrogen, $\varepsilon^{ini} = \sigma^{ini}/E$ is the initial yield strain, and N the hardening exponent, which is assumed to remain unaltered by the presence of hydrogen atoms [53,54]. A possible suggestion for $\sigma^{ini}(c)$ is

$$\sigma^{ini}(c) = ((\chi - 1)c + 1)\sigma^{ini}(0) \tag{12}$$

where $\chi \leq 1$ is a softening parameter. Note that in a continuum sense, Eqs. (11) and (12) imply hydrogen–induced material softening reflecting the experimental observations of hydrogen impact on enhanced dislocation mobility at the micro–scale. Based on the proposed model for including HELP and von Mises yielding with associated flow rule [54,55], the constitutive law taking hydrogen–induced lattice dilatation and material softening into account can be expressed as

$$\sigma_{ij}^{\nabla} = L_{ijkl} D_{kl} \tag{13}$$

where

$$L_{ijkl} = 2G\left[\frac{1}{2}\left(\delta_{ij}\delta_{jl} + \delta_{il}\delta_{jk}\right) - \left[\left(\frac{1}{3}A_2 - \frac{1}{6G}\right)\delta_{ij} + \frac{3A_1}{2\sigma_e^2}\sigma_{ij}^{'}\right]\frac{B_2\sigma_{kl}^{'} - B_1\delta_{kl}}{A_1B_2 - A_2B_1}\left[\frac{1}{3}B_2\delta_{ij} + \frac{9}{4h^{'}\sigma_e^2}\sigma_{ij}^{'}\right]\frac{A_2\sigma_{kl}^{'} - A_1\delta_{kl}}{A_2B_1 - A_1B_2}\right] \tag{14}$$

and

$$A_1 = \frac{\mu\sigma_e}{h^{'}}, \quad A_2 = \frac{1}{3K} + \Lambda(c)\left(\frac{\partial c}{\partial \sigma_{pp}} + \frac{\mu}{h^{'}}\frac{\partial c}{\partial \varepsilon^p}\right) \tag{15}$$

$$B_1 = \frac{1}{2G} + \frac{3}{2h^{'}}, \quad B_2 = \frac{3}{2h^{'}\sigma_e}\Lambda(c)\frac{\partial c}{\partial \varepsilon^p} \tag{16}$$

$$\Lambda(c) = \frac{\lambda}{1 + \lambda(c - c_0)/3}, \quad h^{'} = \frac{\partial \sigma_Y}{\partial \varepsilon^p} + \frac{\partial \sigma_Y}{\partial c}\frac{\partial c}{\partial \varepsilon^p}, \quad \mu = \frac{\partial \sigma_Y}{\partial c}\frac{\partial c}{\partial \sigma_{kk}} \tag{17}$$

in which σ_{ij}^{∇} denotes is the Jaumman rate of the Cauchy stress, δ_{ij} is the Kronecker delta, G and K are the shear and bulk moduli, respectively, D_{ij} is the (symmetric) deformation rate tensor. $\sigma_e = \sqrt{3\sigma_{ij}^{'}\sigma_{ij}^{'}/2}$ is the effective stress, and $\sigma_{ij}^{'} = (\sigma_{ij} - \sigma_{kk}\delta_{ij}/3)$ is the deviatoric stress. The parameter $h^{'}$ denotes the plastic tangent modulus that considers the hydrogen impact on the flow stress, the parameter μ is the corresponding pressure sensitivity of yield, $\lambda = \Delta\nu/\Psi$ with $\Delta\nu = V_H/N_A$ and Ψ respectively being the volume increase per hydrogen atom and mean atomic volume of the host lattice.

4. Cohesive–interface elements

The cohesive–interface elements provide a computationally efficient tool to model damage taking place in a fracture process zone (FPZ) located ahead of a crack tip. This approach, which includes nonlinear constitutive laws characterized by the displacement jump and the corresponding cohesive traction along the cohesive surfaces, furnishes a phenomenological model to simulate crack nucleation, initiation, and propagation. To be able to model hydrogen–induced degradation, a key issue in cohesive–interface elements is the determination of the TSL characterizing the response of the degraded cohesive elements.

4.1. PPR potential–based model

In the present work, the PPR potential–based model [39] is adopted as the TSL. Using the PPR model, the hydrogen degradation process can be controlled by changing the ductility, from a convex brittle to a concave ductile shape, in addition to lowering the cohesive strength and/or fracture energy. This can be achieved by an appropriate choice of four physical fracture parameters in each fracture mode including fracture energy, cohesive strength, shape, and initial slope.

While solid elements model the bulk material, which follows a finite–strain, incremental plasticity (Mises) constitutive model, the cohesive–interface elements are governed by the PPR model. This work employs the intrinsic implementation [40], in which the cohesive–interface elements are inserted into the bulk element mesh to capture the crack propagation process, as depicted in Fig. 1. The PPR potential, Ψ, a function of normal and tangential separations, Δ_n and Δ_t, is expressed as [39]:

$$\Psi(\Delta_n, \Delta_t) = \min(\varphi_n, \varphi_t) + \left(\Gamma_n\left(1 - \frac{\Delta_n}{\delta_n}\right)^{\overline{\alpha}}\left(\frac{m}{\overline{\alpha}} + \frac{\Delta_n}{\delta_n}\right)^m + \left\langle \varphi_n - \varphi_t \right\rangle\right) \times \left(\Gamma_t\left(1 - \frac{|\Delta_t|}{\delta_t}\right)^{\overline{\beta}}\left(\frac{n}{\overline{\beta}} + \frac{|\Delta_t|}{\delta_t}\right)^n + \left\langle \varphi_t - \varphi_n \right\rangle\right) \tag{18}$$

where $\langle\rangle$ denotes the Macauley bracket, $\overline{\alpha}$ and $\overline{\beta}$ are the shape parameters. Γ_n and Γ_t are energy constants, φ_n and φ_t denote fracture energies in Mode I and Mode II obtained from the areas under the traction separation curve in normal and tangential separation, respectively. λ_n and λ_t are the initial stiffness indicators, and $\overline{\alpha}$ and $\overline{\beta}$ are shape parameters. Appendix A elaborates the present implementation with traction vectors $T_n(\Delta_n, \Delta_t)$ and $T_t(\Delta_n, \Delta_t)$ in normal and tangential direction along with relevant parameters.

4.2. Implementing hydrogen effect

What makes the cohesive technique particularly appealing in the numerical modelling of hydrogen–induced degradation is the possibility

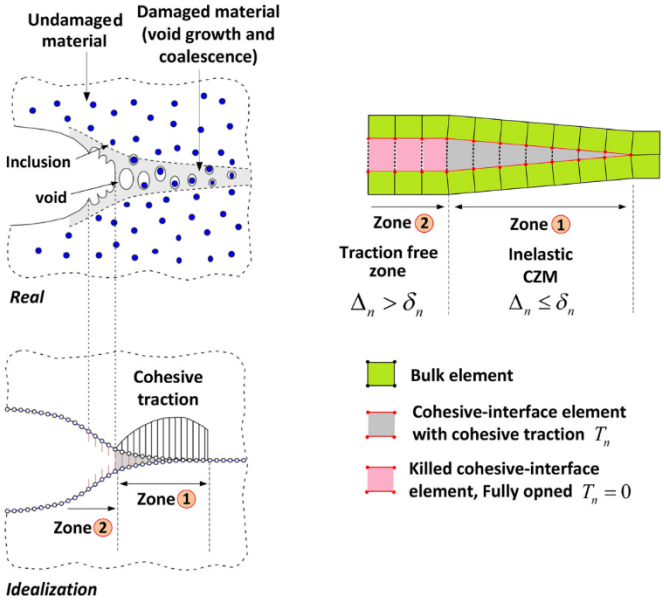

Fig. 1. Intrinsic implementation of the PPR potential-based cohesive–interface elements.

of implementing degraded TSL, which represents hydrogen degradation of the material. Using a renormalization procedure [56,57] in order to scale the atomic–level cohesive properties up to the continuum scale, Serebrinsky et al. [35] implemented the HEDE approach in a CZM of fracture, explaining the impact of hydrogen segregation by a quantum–mechanical treatment. Established on the formulation presented by Jiang and Carter [7] on the ideal cleavage energy of Fe and Al in the presence of various hydrogen amounts, the following coupling between hydrogen coverage, ϕ_H, and the critical cohesive traction (cohesive strength), T_c, has been suggested as

$$T_c(\phi_H) = T_c(0)\left(1 - 1.0467\phi_H + 0.1687\phi_H^2\right) \tag{19}$$

where $T_c(0)$ denotes the critical cohesive traction with no hydrogen influence. To correlate the total bulk hydrogen concentration C with the hydrogen coverage, the Langmuir–McLean isotherm [58] is applied as

$$\phi_H = \frac{C}{C + \exp\left(-\Delta G_b^0/RT\right)} \tag{20}$$

where G_b^0 is the Gibbs energy difference between surface and bulk material. In contrast to the approach used by Raykar et al. [18] and Vergani et al. [59], where a hydrogen damaging effect both on the cohesive strength and on the critical separation was considered, in the present work, a linear dependence on hydrogen concentration according to Eq. (19) is chosen only for the critical cohesive traction. In addition, the value of the cohesive energy of the PPR–based TSL is adopted from the experimental data of hydrogen–charged specimen.

5. Finite element (FE) computational model

It is evident from Eqs. (8) and (13) that the hydrogen transport and the elastoplastic boundary–value problems are fully coupled. Hence, the solution involves iteration and the FE procedure, which are performed here using a research code, WARP3D [60]. This code incorporates 8–node isoparametric solid elements and the zero thickness 8–node cohesive–interface elements, which include two 4–node bilinear isoparametric surfaces and connect the faces of compatible solid elements. A graphic representation of the entire numerical modelling procedure is depicted in the flowchart in Fig. 2.

Full details of the FE model for a C(T) specimen is demonstrated in Fig. 3. As can be seen, crack growth takes place through the 8–node cohesive elements placed along the symmetry plane, where cohesive–interface elements reside only over the initial uncracked ligament, thereby constraining propagation in the Mode I configuration. Accordingly, $v = 0$, where v is the displacement in the y direction, at all nodes of the cohesive–interface elements on the symmetry line. In addition, plane–strain conditions are invoked with $w = 0$ at all nodes, where w denotes the displacement in the z direction [60]. Furthermore, the cohesive element extinction begins when the normal separation at every integration point of the element exceeds 0.9 fraction of the final

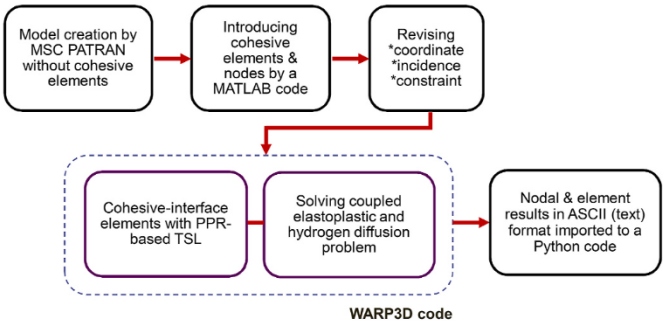

Fig. 2. Flowchart of numerical modelling procedure proposed for prediction of HE.

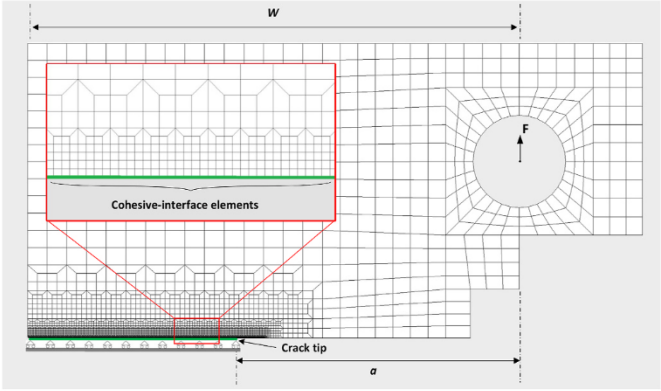

Fig. 3. Finite element model including zero thickness cohesive–interface elements incorporating ductile tearing for the C(T) specimen with $a/W = 0.6$.

separation in the normal direction, δ_n. In this work, the nonlinear FE analysis incorporating ductile crack growth deals with a plane–strain model of a C(T) fracture specimen with $a/W = 0.6$, where the crack length (a) and the width ($W = 25$ mm) are measured from load line. In this work, the initial and boundary conditions for the diffusion problem have been considered according to the experimental testing conditions [61]. The specimen is supposed to be initially free of hydrogen, as such the initial condition $C_L(x, y, z, 0) = 0$ is adopted. To simulate cathodic charging, C_L is maintained as C_L^{ini} on all free surfaces of the specimen.

The AISI 4130 high strength steel used in the present analysis has a yield stress of 715 MPa, Young's Modulus of 220 GPa, and a Poisson's ratio of 0.3. Table 2 shows the measured, uniaxial true stress versus logarithmic strain values for the material. This segmental form of the stress–strain curve serves as input for the finite–strain, incremental plasticity model for the bulk material.

6. Numerical results and discussion

Having been established the computational model, in this section, firstly parameters involved in the hydrogen–degraded PPR model are properly calibrated with experimental data for the uncharged and hydrogen–charged C(T) specimens. Note that in this study, the results after time 130 s [47], which time has no effect on the hydrogen concentration, will be discussed. The role of the softening shape parameter is investigated. Afterwards, the impact of hydrogen concentration on the hydrogen coverage profile ahead of the crack tip is studied in detail. Then, the crack growth resistance curves for the uncharged and hydrogen–charged C(T) specimens are obtained. Last but not least, we will assess the distribution of stress triaxiality ahead of crack tip as a function of the NILS hydrogen contents and hydrogen–induced softening.

A series of simulations for the FE model of the C(T) specimen having one layer of the element over the half-thickness have been performed. The analyses investigate several combinations of in–plane mesh refinement with interface element sizes, L_e, and properties of the PPR model

Table 2
Experimental true stress–logarithmic strain curve for AISI 4130 high strength steel [61].

σ (MPa)	Log strain
736.74	0.001
879.70	0.015
964.25	0.035
1062.35	0.080
1187.61	0.200
1330.14	0.500
1410.23	0.800
1431.08	0.900

(T_c and φ_n). These studies reveal that large value of the L_e not only fail to resolve strain–stress fields in the plastically deforming bulk material modeled with solid elements, but also can lead to oscillating, non–convergent cycles of the global Newton solution. To obtain converged Newton iterations over the entire history of loading, the analyses suggest that $L_e \leq 3\delta_n$. In following numerical results, the cohesive–interface elements in the direction of crack growth have the mesh size of $L_e = 0.1563$ μm to ensure proper resolution of results. Sung et al. [23] used an approach of choosing the cohesive energy as the J–integral at crack initiation, which is defined when the load–displacement curve initiates to deviate from the experimental one. However, detecting the location of crack initiation is somehow questionable. It is because the trapezoidal TSL used has a linear softening behavior with limited number of parameters to fit properly with the experimental results. In contrast, in the present study, the proposed PPR model, which has four physical fracture parameters including cohesive energy, cohesive strength, shape, and initial slope, enables flexibility in the softening shape in TSL. Accordingly, the numerical results are fittingly matched with experimental results. As shown in Fig. 4, a best fit to the load–displacement curve is achieved for a cohesive strength of 2250 MPa and 615 MPa for the uncharged and hydrogen–charged C(T) specimens, respectively. The corresponding cohesive energy 215.5 kJ/m^2 and 22 kJ/m^2 for the uncharged and hydrogen–charged tests, respectively, is determined based solely on the experimental test, similar to the procedure proposed by Roychowdhury et al. [62]. To adequately calibrate the PPR model with experimental data in Fig. 4, the shape parameter is determined as $\overline{\alpha} = 2.7$ and $\overline{\alpha} = 3$ for the uncharged and hydrogen–charged specimens, respectively. Also, $\lambda_n = 0.01$ is adopted for both conditions.

To clarify the role of the softening shape parameter in hydrogen–degraded PPR model, firstly, the effect of $\overline{\alpha}$ on the traction–separation curve for Mode I is studied in Fig. 5. Note that the degradation process in the PPR model is achieved by two ways; by reducing the critical cohesive strength and by changing the softening shape parameter, $\overline{\alpha}$, which alters the softening shape of the TSL. It can be inferred from Fig. 5 that increasing the shape parameter, the softening part of the TSL transforms from a convex brittle ($\overline{\alpha} > 2$) into a concave ductile ($\overline{\alpha} < 2$) shape, plateau–like post–peak behavior. It is interesting to note that selecting $\overline{\alpha} = 2$ leads the PPR model to the triangular TSL. The variation of the applied load with load–line displacement for different values of the softening shape parameter is shown in Fig. 6. This figure demonstrates the capability of the hydrogen–degraded PPR model to properly calibrate the numerical result obtained with that of experimental test.

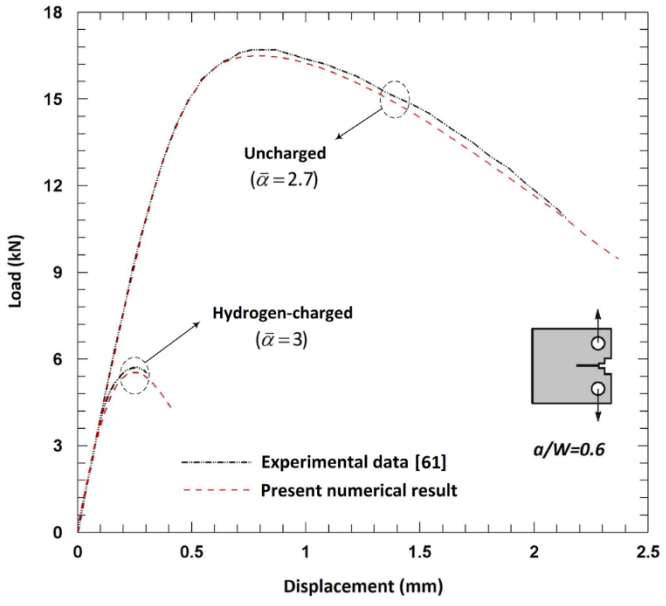

Fig. 4. Comparison between experimental and numerical results with calibrated parameters for the uncharged and hydrogen–charged C(T) specimens.

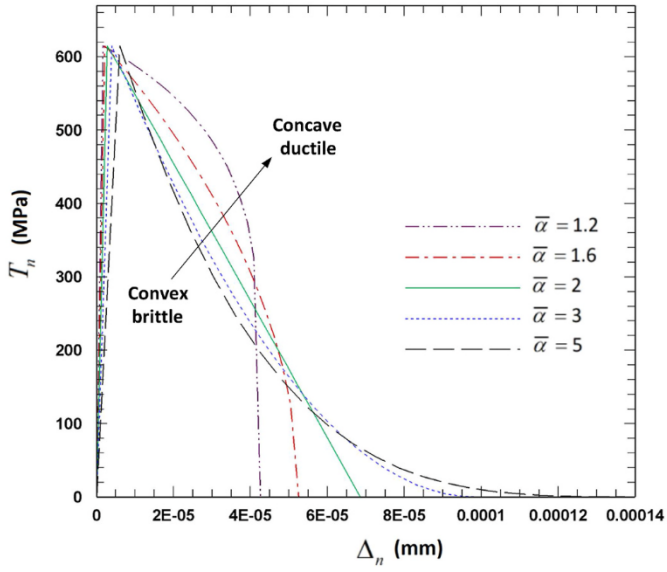

Fig. 5. Influence of softening shape parameters on the hydrogen–degraded traction–separation curve ($\lambda_n = 0.01$).

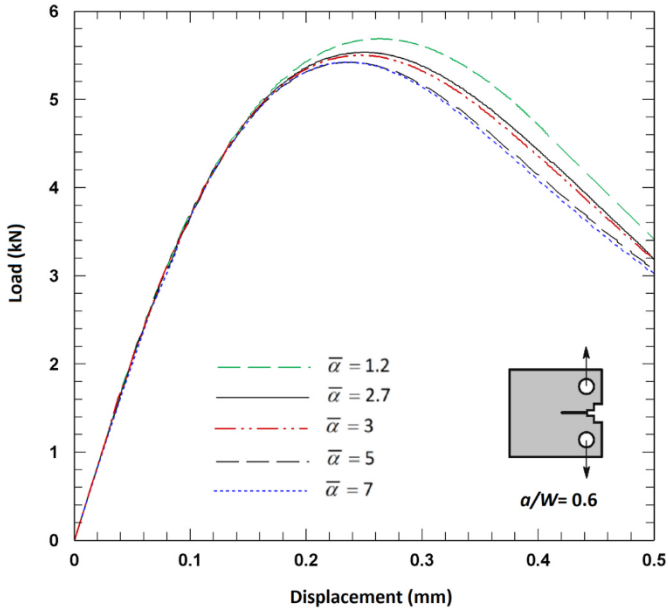

Fig. 6. Impact of softening shape parameters involved in PPR model on the load–displacement curve ($\lambda_n = 0.01$).

In Fig. 7 the effect of hydrogen concentration on the hydrogen coverage profile ahead of the crack tip is demonstrated. In this figure, the hydrogen coverage is determined in terms of either the lattice hydrogen concentration, $c = c_L$, or total hydrogen concentration, $c = c_L + c_T$. As can be seen, trapped hydrogen has a negligible influence on the trend of the evolution of the hydrogen coverage profile ahead of the crack tip for various values of the initial NILS concentration. It can be concluded from Fig. 7 that the lattice hydrogen has the dominating factor in the hydrogen degradation compared with trapped hydrogen. Similar finding has been reported by Ayas et al. [45]. Notwithstanding, Novak et al. [10] conjectured that low–binding energy dislocation traps

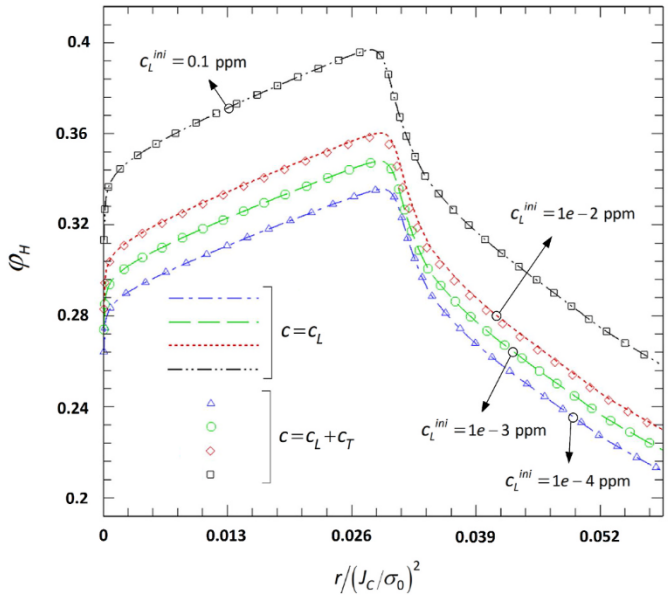

Fig. 7. Effect of initial lattice hydrogen concentration on the hydrogen coverage profile ahead of the crack tip just prior to the onset of crack propagation ($\chi = 1$).

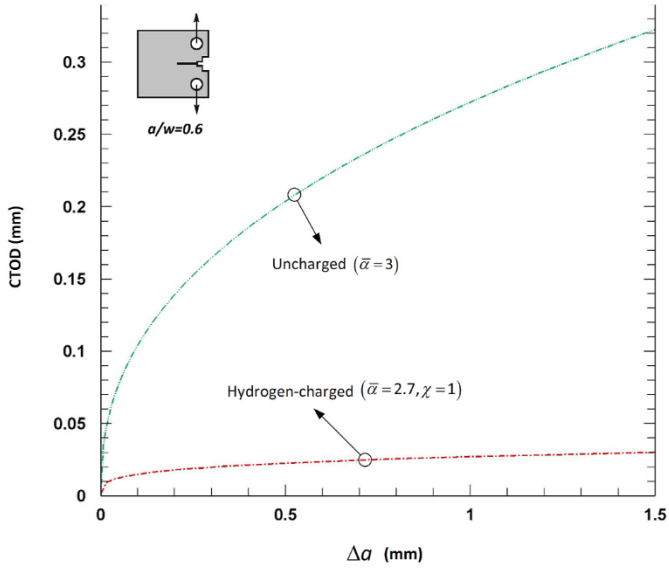

Fig. 8. CTOD R–curves for the uncharged and hydrogen–charged C(T) specimens ($\lambda_n = 0.01$).

have the leading contribution to promoting hydrogen–induced fracture. Furthermore, Jemblie et al. [24] found that the level of trap binding energy in excess of 23 kJ/mol plays a crucial role in making the dislocation trap sites being dominant factor in hydrogen degradation. As can be observed in Fig. 7, the peak of hydrogen coverage profile increases and tends to the crack tip with increase in initial lattice hydrogen concentration. For $c_L^{ini} = 0.1$ ppm, a maximum coverage of 39.68% is reached at the hydrogen coverage peak.

The crack tip opening displacement (CTOD) R–curves, measured in terms of δ_5 [63] versus crack extension (Δa), for the uncharged and hydrogen–charged C(T) specimens are presented in Fig. 8. The so–called "δ_5" is obtained as the displacement of two points located at 2.5 mm above and below the crack tip prior to the onset of crack propagation. Note that herein just one point has been considered due to the symmetry

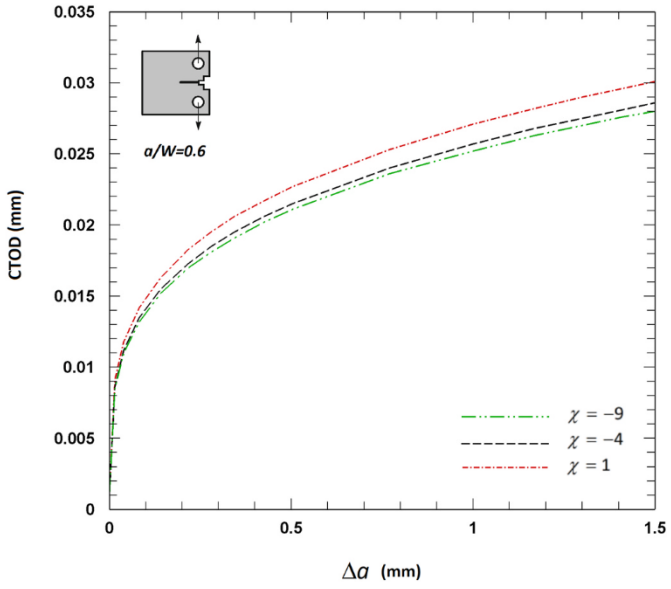

Fig. 9. Effect of hydrogen–induced softening on the CTOD R–curves for the hydrogen–charged specimen ($c_L^{ini} = 0.01$ ppm).

model. From this figure, one can find that the lower CTOD R–curve for the hydrogen–charged specimen shows the significant degradation impact of hydrogen on the ductility of the steel material, similar trend observed in the experimental work conducted by Scheider et al. [17]. As shown in Fig. 8, the value of CTOD at crack initiation for the hydrogen–charged specimen drastically decreases by 90.6%.

The effect of hydrogen–induced softening on the CTOD R–curves for the hydrogen–charged specimen is shown in Fig. 9. One can deduce from Eq. (12) that when $\chi = 1$, the material does not soften. Moreover, a −9 value for χ is associated with 10% reduction of the initial yield stress at the initial concentration of hydrogen in NILS before the application of the load, and a −4 value for χ denotes a 5% reduction in the initial yield stress [11,53]. As can be seen from Fig. 9, by decreasing the softening parameter, or in other words, rising hydrogen–induced softening effect, CTOD values appreciably decline with crack growth. Another point that

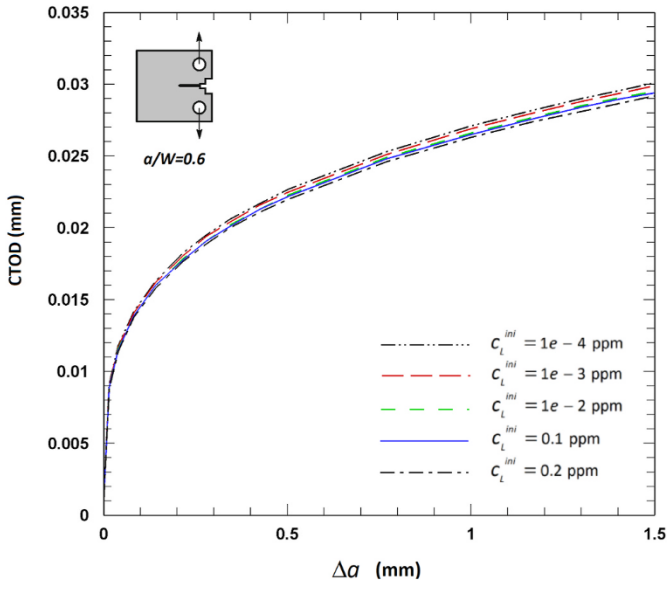

Fig. 10. Variation of CTOD R–curves for the hydrogen–charged specimen with initial NILS hydrogen concentration ($\chi = 1$).

can be found from this figure is that as the crack grows, the impact of hydrogen–induced softening on the CTOD values becomes more pronounced. In Fig. 10 variation of CTOD R–curves for the hydrogen–charged specimen with initial NILS hydrogen concentration is presented. It can be observed that hydrogen–induced lowering of the CTOD values is markedly noticeable with incense of the initial lattice hydrogen concentration. In addition, by the evolution of the crack extension, the impact of NILS concentration of hydrogen on the CTOD values increases.

In the following discussion, we turn our attention to the investigation of the distribution of stress triaxiality ahead of crack tip with the NILS hydrogen contents and hydrogen–induced softening. The quantity σ_{kk}/σ_e defines a convenient measure of stress triaxiality linked to the crack growth rate of micro–scale voids, where σ_{kk} denotes the hydrostatic stress and σ_e is the von Mises stress. Fig. 11 depicts the variation of stress triaxiality ahead of the crack tip with initial lattice hydrogen concentration, taken only before the crack initiates. As can be seen from this figure, the apex of the triaxiality noticeably declines by increasing the initial NILS concentration, followed by shifting towards the crack tip. However, it is worth noting that the impact of NILS concentration of hydrogen on the stress triaxiality becomes less appreciable by receding from the crack tip. Furthermore, the evolution of stress triaxiality ahead of the crack tip with hydrogen–induced softening just prior to the onset of crack propagation is displayed in Fig. 12. It is inferred from this plot that decreasing softening parameter from 1 to −9 and −4 value, the apex of the stress triaxiality decreases by 18.3% and 30.9%, respectively. It is interesting to note that comparing Figs. 7 and 12 reveals that high hydrogen concentrations are located in the same places as high stress triaxiality.

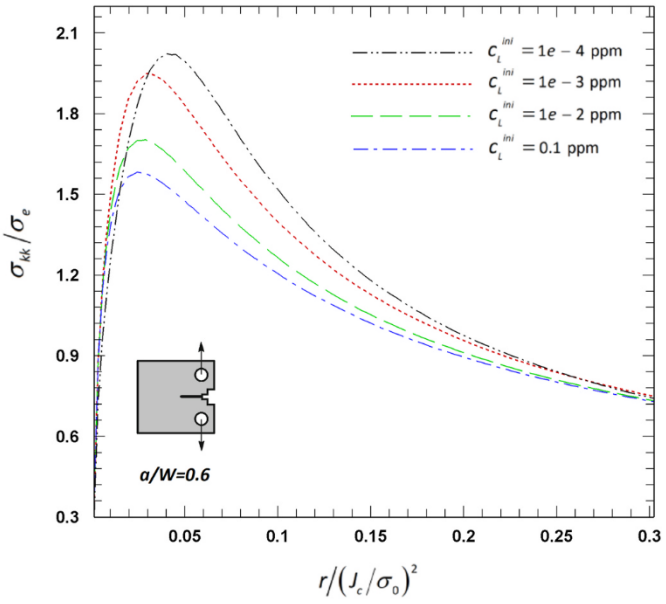

Fig. 11. Variation of stress triaxiality ahead of the crack tip with initial lattice hydrogen concentration just prior to the onset of crack growth ($\chi = 1$).

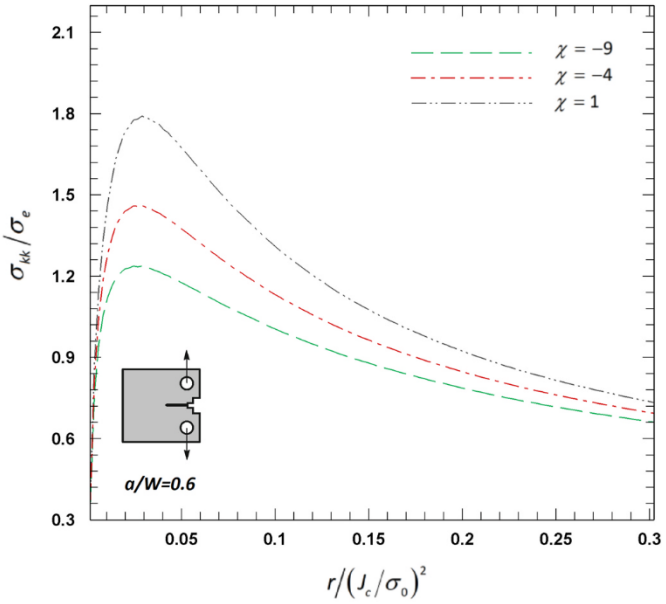

Fig. 12. Evolution of stress triaxiality ahead of the crack tip with hydrogen–induced softening just prior to the crack initiation ($c_L^{ini} = 0.0016$ ppm).

7. Conclusion

This study presented a fully coupled CZM–based computational framework to model ductile crack extension in high strength steels. The model has comprised initially zero thickness, cohesive–interface elements with constitutive response described by a hydrogen–degraded PPR model. The linear dependence on hydrogen concentration according to a phenomenological decohesion model was chosen only for the critical cohesive traction. Moreover, the value of the cohesive energy of the PPR–based TSL was adopted from the experimental data of hydrogen–charged specimen. The computational framework accounting for both HEDE and HELP mechanisms was employed to simulate ductile crack extension in a C(T) specimen made of AISI 4130 high strength steel. The parameters included in the PPR model were satisfactorily calibrated with experimental data for the uncharged and hydrogen–charged specimens. The authors encourage the extension of present work to include more effects in the model, such as size effects and diffusion effect on the plastic deformation. The main results can be summarised as follows:

- The degradation process in the PPR model has been achieved by two ways; by reducing the critical cohesive strength and by changing the softening shape parameter, which alters the softening shape of the TSL. The results show that increasing the shape parameter, the softening part of the TSL transforms from a convex brittle into a concave ductile shape, plateau–like post–peak behavior.
- Based on the results obtained for AISI 4130 high strength steels, it has been concluded that the lattice hydrogen has the dominating factor in the hydrogen degradation compared with trapped hydrogen.
- Numerical results show that increasing hydrogen–induced softening effect, CTOD values appreciably decline with crack growth. Furthermore, it has been observed that as the crack grows, the impact of hydrogen–induced softening on the CTOD values becomes more pronounced.
- It has been inferred that the lower CTOD R–curve, decreased by 90.6% at the crack initiation point, for the hydrogen–charged specimen shows the significant degradation impact of hydrogen on the ductility of the steel material.
- Results reveal that the apex of the stress triaxiality noticeably declines by increasing the initial NILS concentration, followed by shifting towards the crack tip. Notwithstanding, the impact of NILS concentration of hydrogen on the stress triaxiality becomes less appreciable by receding from the crack tip.

CRediT authorship contribution statement

B. Sobhaniaragh: Conceptualization, Formal analysis, Methodology, Software, Formal analysis, Validation, Writing - original draft, Writing - review & editing, Funding acquisition. **S.H. Afzalimir:** Formal analysis, Investigation, Methodology, Validation, Writing - review & editing. **C. Ruggieri:** Supervision, Writing - review & editing, Funding acquisition.

Declaration of competing interest

The authors declare that they have no known competing financial interests or personal relationships that could have appeared to influence the work reported in this paper.

Acknowledgment

This work has been supported by Fundação de Amparo à Pesquisa do Estado de São Paulo (FAPESP) through research grant 2018/23217-9.

Appendix A

The gradient of Eq. (18) results in the traction vectors as

$$T_n(\Delta_n,\Delta_t)=\frac{\partial\Psi}{\partial\Delta_n}= \frac{\Gamma_n}{\delta_n}\left(m\left(1-\frac{\Delta_n}{\delta_n}\right)^{\overline{\alpha}}\left(\frac{m}{\overline{\alpha}}+\frac{\Delta_n}{\delta_n}\right)^{m-1}-\overline{\alpha}\left(1-\frac{\Delta_n}{\delta_n}\right)^{\overline{\alpha}-1}\left(\frac{m}{\overline{\alpha}}+\frac{\Delta_n}{\delta_n}\right)^{m}\right)\times\left(\Gamma_t\left(1-\frac{|\Delta_t|}{\delta_t}\right)^{\overline{\beta}}\left(\frac{n}{\overline{\beta}}+\frac{|\Delta_t|}{\delta_t}\right)^{n}+\langle\phi_t-\phi_n\rangle\right) \tag{A.1}$$

$$T_t(\Delta_n,\Delta_t)=\frac{\partial\Psi}{\partial\Delta_t}= \frac{\Gamma_t}{\delta_t}\left(n\left(1-\frac{|\Delta_t|}{\delta_t}\right)^{\overline{\beta}}\left(\frac{n}{\overline{\beta}}+\frac{|\Delta_t|}{\delta_t}\right)^{n-1}-\overline{\beta}\left(1-\frac{|\Delta_t|}{\delta_n}\right)^{\overline{\beta}-1}\left(\frac{n}{\overline{\beta}}+\frac{|\Delta_t|}{\delta_t}\right)^{n}\right)\times\left(\Gamma_n\left(1-\frac{\Delta_n}{\delta_n}\right)^{\overline{\alpha}}\left(\frac{m}{\overline{\alpha}}+\frac{\Delta_n}{\delta_n}\right)^{m}+\langle\phi_n-\phi_t\rangle\right)\ \frac{\Delta_t}{|\Delta_t|} \tag{A.2}$$

where energy parameters in Mode I and Mode II, Γ_n and Γ_t, respectively, are given by

$$\Gamma_n=(-\varphi_n)^{\frac{\langle\varphi_n-\varphi_t\rangle}{\varphi_n}\frac{\langle\varphi_t-\varphi_n\rangle}{\varphi_t}}\left(\frac{\overline{\alpha}}{m}\right)^{m},\ \Gamma_t=(-\varphi_t)^{\frac{\langle\varphi_t-\varphi_n\rangle}{\varphi_t}\frac{\langle\varphi_n-\varphi_t\rangle}{\varphi_n}}\left(\frac{\overline{\beta}}{n}\right)^{n},\ \text{for}\ (\varphi_n\neq\varphi_t) \tag{A.3}$$

and

$$\Gamma_n=-\varphi_n\left(\frac{\overline{\alpha}}{m}\right)^{m},\ \Gamma_t=\left(\frac{\overline{\beta}}{n}\right)^{n},\ \text{for}\ (\varphi_n=\varphi_t) \tag{A.4}$$

The fracture energies in Mode I, φ_n, and Mode II, φ_t, obtained from the areas under the traction separation curve in normal and tangential separation, respectively, are expressed by

$$\varphi_n=\int_0^{\delta n}\delta_n T_n(\Delta_n,0)d\Delta_n\ ,\quad \varphi_t=\int_0^{\delta t}\delta_t T_t(0,\Delta_t)d\Delta_t \tag{A.5}$$

The initial stiffness indicators, λ_n and λ_t, are defined as the ratio of the opening and sliding displacements at the peak traction values (start of softening) to the values when the tractions degrade to zero as

$$\lambda_n=\frac{\delta_{nc}}{\delta_n},\quad \lambda_t=\frac{\delta_{tc}}{\delta_t} \tag{A.6}$$

Furthermore, the non-dimensional exponents, m and n, are given by

$$m=\frac{\overline{\alpha}(\overline{\alpha}-1)\lambda_n^2}{\left(1-\overline{\alpha}\lambda_n^2\right)},\quad n=\frac{\overline{\beta}(\overline{\beta}-1)\lambda_t^2}{\left(1-\overline{\beta}\lambda_t^2\right)} \tag{A.7}$$

The final separation in the normal and tangential directions are expressed by

$$\delta_n=\frac{\varphi_n}{T_{nc}}\overline{\alpha}\lambda_n(1-\lambda_n)^{\overline{\alpha}-1}\left(\frac{\overline{\alpha}}{m}+1\right)\left(\frac{\overline{\alpha}}{m}\lambda_n+1\right)^{m-1} \tag{A.8}$$

$$\delta_t=\frac{\varphi_t}{T_{tc}}\overline{\beta}\lambda_t(1-\lambda_t)^{\overline{\beta}-1}\left(\frac{\overline{\beta}}{n}+1\right)\left(\frac{\overline{\beta}}{n}\lambda_t+1\right)^{n-1} \tag{A.9}$$

in which T_{nc} and T_{nt} denote the critical cohesive tractions in normal and tangential directions. In addition, the conjugates $\overline{\delta}_n$ and $\overline{\delta}_t$ are extracted by solving the following equations [39].

$$\Gamma_n\left(1-\frac{\overline{\delta}_n}{\delta_n}\right)^{\overline{\alpha}}\left(\frac{m}{\overline{\alpha}}+\frac{\overline{\delta}_n}{\delta_n}\right)^{m}+\langle\varphi_n-\varphi_t\rangle=0 \tag{A.10}$$

$$\Gamma_t\left(1-\frac{\overline{\delta}_t}{\delta_t}\right)^{\overline{\beta}}\left(\frac{n}{\overline{\beta}}+\frac{\overline{\delta}_t}{\delta_t}\right)^{n}+\langle\varphi_t-\varphi_n\rangle=0 \tag{A.11}$$

References

[1] E. Ohaeri, U. Eduok, J. Szpunar, Hydrogen related degradation in pipeline steel: a review, Int. J. Hydrogen Energy 43 (31) (2018) 14584–14617.
[2] M. Dadfarnia, A. Nagao, S. Wang, M.L. Martin, B.P. Somerday, P. Sofronis, Recent advances on hydrogen embrittlement of structural materials, Int. J. Fract. 196 (2015) 223–243.
[3] I.M. Robertson, P. Sofronis, A. Nagao, M.L. Martin, S. Wang, D.W. Gross, K. E. Nygren, Hydrogen embrittlement understood, Metall. Mater. Trans. 46A (2015) 2323–2341.
[4] J. Ogden, A.M. Jaffe, D. Scheitrum, Z. McDonald, M. Miller, Natural gas as a bridge to hydrogen transportation fuel: insights from the literature, Energy Pol. 115 (2018) 317–329.
[5] O. Barrera, D. Bombac, Y. Chen, T. Daff, E. Galindo-Nava, P. Gong, D. Haley, R. Horton, I. Katzarov, J. Kermode, et al., Understanding and mitigating hydrogen embrittlement of steels: a review of experimental, modelling and design progress from atomistic to continuum, J. Mater. Sci. 53 (9) (2018) 6251–6290.
[6] R. Hoagland, H. Heinisch, An atomic simulation of the influence of hydrogen on the fracture behavior of nickel, J. Mater. Res. 7 (8) (1992) 2080–2088.
[7] D. Jiang, E.A. Carter, First principles assessment of ideal fracture energies of materials with mobile impurities: implications for hydrogen embrittlement of metals, Acta Mater. 52 (16) (2004) 4801–4807.
[8] T. Lee, I. Robertson, H. Birnbaum, An hvem in situ deformation study of nickel doped with sulfur, Acta Metall. 37 (2) (1989) 407–415.
[9] A. Barnoush, H. Vehoff, Electrochemical nanoindentation: a new approach to probe hydrogen/deformation interaction, Scripta Mater. 55 (2) (2006) 195–198.
[10] P. Novak, R. Yuan, B. Somerday, P. Sofronis, R. Ritchie, A statistical, physical-based, micro-mechanical model of hydrogen-induced intergranular fracture in steel, J. Mech. Phys. Solid. 58 (2) (2010) 206–226.
[11] D. Ahn, P. Sofronis, R. Dodds, Modeling of hydrogen-assisted ductile crack propagation in metals and alloys, Int. J. Fract. 145 (2) (2007) 135–157.
[12] Y. Liang, D. Ahn, P. Sofronis, R. Dodds Jr., D. Bammann, Effect of hydrogen trapping on void growth and coalescence in metals and alloys, Mech. Mater. 40 (3) (2008) 115–132.
[13] M. Dadfarnia, P. Sofronis, T. Neeraj, Hydrogen interaction with multiple traps: can it be used to mitigate embrittlement? Int. J. Hydrogen Energy 36 (16) (2011) 10141–10148.
[14] J.-Y. Wu, T.K. Mandal, V.P. Nguyen, A phase-field regularized cohesive zone model for hydrogen assisted cracking, Comput. Methods Appl. Mech. Eng. 358 (2020) 112614.
[15] A. Alvaro, V. Olden, O.M. Akselsen, 3d cohesive modelling of hydrogen embrittlement in the heat affected zone of an x70 pipeline steel, Int. J. Hydrogen Energy 38 (18) (2013) 7539–7549.
[16] N. Raykar, S. Maiti, R.S. Raman, Modelling of mode-i stable crack growth under hydrogen assisted stress corrosion cracking, Eng. Fract. Mech. 78 (18) (2011) 3153–3165.
[17] I. Scheider, M. Pfuff, W. Dietzel, Simulation of hydrogen assisted stress corrosion cracking using the cohesive model, Eng. Fract. Mech. 75 (15) (2008) 4283–4291.
[18] N.R. Raykar, S.K. Maiti, R.S. Raman, S. Aryan, Study of hydrogen concentration dependent growth of external annular crack in round tensile specimen using cohesive zone model, Eng. Fract. Mech. 106 (2013) 49–66.
[19] H. Yu, J.S. Olsen, A. Alvaro, V. Olden, J. He, Z. Zhang, A uniform hydrogen degradation law for high strength steels, Eng. Fract. Mech. 157 (2016) 56–71.
[20] G. Gobbi, C. Colombo, S. Miccoli, L. Vergani, A weakly coupled implementation of hydrogen embrittlement in fe analysis, Finite Elem. Anal. Des. 141 (2018) 17–25.
[21] T. Siegmund, W. Brocks, A numerical study on the correlation between the work of separation and the dissipation rate in ductile fracture, Eng. Fract. Mech. 67 (2) (2000) 139–154.
[22] A. Díaz, J. Alegre, I. Cuesta, Numerical simulation of hydrogen embrittlement and local triaxiality effects in notched specimens, Theor. Appl. Fract. Mech. 90 (2017) 294–302.
[23] S.-J. Sung, J. Pan, P.S. Korinko, M. Morgan, A. McWillliams, Simulations of fracture tests of uncharged and hydrogen-charged additively manufactured 304 stainless steel specimens using cohesive zone modeling, Eng. Fract. Mech. 209 (2019) 125–146.
[24] L. Jemblie, V. Olden, P. Mainçon, O.M. Akselsen, Cohesive zone modelling of hydrogen induced cracking on the interface of clad steel pipes, Int. J. Hydrogen Energy 42 (47) (2017) 28622–28634.
[25] Z. Xia, B. Wang, J. Zhang, S. Ding, L. Chen, H. Pang, X. Song, Three-dimensional numerical simulation of hydrogen-induced multi-field coupling behavior in cracked zircaloy cladding tubes, Nuclear Engineering and Technology 51 (1) (2019) 238–248.
[26] E. Martínez-Pañeda, A. Golahmar, C.F. Niordson, A phase field formulation for hydrogen assisted cracking, Comput. Methods Appl. Mech. Eng. 342 (2018) 742–761.
[27] V. Olden, A. Alvaro, O.M. Akselsen, Hydrogen diffusion and hydrogen influenced critical stress intensity in an api x70 pipeline steel welded joint–experiments and fe simulations, Int. J. Hydrogen Energy 37 (15) (2012) 11474–11486.
[28] A. Alvaro, V. Olden, O.M. Akselsen, 3d cohesive modelling of hydrogen embrittlement in the heat affected zone of an x70 pipeline steel–part ii, Int. J. Hydrogen Energy 39 (7) (2014) 3528–3541.
[29] A. Traidia, M. Alfano, G. Lubineau, S. Duval, A. Sherik, An effective finite element model for the prediction of hydrogen induced cracking in steel pipelines, Int. J. Hydrogen Energy 37 (21) (2012) 16214–16230, advances in Hydrogen Production (Selected papers from ICH2P-2011).
[30] D. De Meo, C. Diyaroglu, N. Zhu, E. Oterkus, M.A. Siddiq, Modelling of stress-corrosion cracking by using peridynamics, Int. J. Hydrogen Energy 41 (15) (2016) 6593–6609.
[31] J. Palma Carrasco, D. Silva Diniz, J. Andrade Barbosa, A. Almeida Silva, Numerical modeling of hydrogen diffusion in structural steels under cathodic overprotection and its effects on fatigue crack propagation, Mater. Werkst. 43 (5) (2012) 392–398.
[32] K. Saliya, B. Panicaud, C. Labergère, Advanced modeling and numerical simulations for the thermo-chemico-mechanical behaviour of materials with damage and hydrogen, based on the thermodynamics of irreversible processes, Finite Elem. Anal. Des. 164 (2019) 79–97.
[33] S. Suman, M.K. Khan, M. Pathak, R. Singh, 3d simulation of hydride-assisted crack propagation in zircaloy-4 using xfem, Int. J. Hydrogen Energy 42 (29) (2017) 18668–18673.
[34] G. Gobbi, C. Colombo, S. Miccoli, L. Vergani, A fully coupled implementation of hydrogen embrittlement in fe analysis, Adv. Eng. Software 135 (2019) 102673.
[35] S. Serebrinsky, E. Carter, M. Ortiz, A quantum-mechanically informed continuum model of hydrogen embrittlement, J. Mech. Phys. Solid. 52 (10) (2004) 2403–2430.
[36] L. Jemblie, V. Olden, O.M. Akselsen, A review of cohesive zone modelling as an approach for numerically assessing hydrogen embrittlement of steel structures, Phil. Trans. Math. Phys. Eng. Sci. 375 (2098) (2017) 20160411.
[37] S. Wu, S.-J. Sung, J. Pan, P.-S. Lam, M.J. Morgan, P.S. Korinko, Modeling of crack extensions in arc-shaped specimens of hydrogen-charged austenitic stainless steels using cohesive zone model, in: ASME 2018 Pressure Vessels and Piping Conference, American Society of Mechanical Engineers Digital Collection, 2018.
[38] S. Pallaspuro, H. Yu, A. Kisko, D. Porter, Z. Zhang, Fracture toughness of hydrogen charged as-quenched ultra-high-strength steels at low temperatures, Mater. Sci. Eng., A 688 (2017) 190–201.
[39] K. Park, G.H. Paulino, J.R. Roesler, A unified potential-based cohesive model of mixed-mode fracture, J. Mech. Phys. Solid. 57 (6) (2009) 891–908.
[40] A. Cerrone, P. Wawrzynek, A. Nonn, G.H. Paulino, A. Ingraffea, Implementation and verification of the park–paulino–roesler cohesive zone model in 3d, Eng. Fract. Mech. 120 (2014) 26–42.
[41] K. Park, G. H. Paulino, Cohesive zone models: a critical review of traction-separation relationships across fracture surfaces, Appl. Mech. Rev. 64 (6).
[42] R.P. Gangloff, Hydrogen Assisted Cracking of High Strength Alloys, Tech. Rep, Aluminum Co of America Alcoa Center Pa Alcoa Technical Center, 2003.
[43] D. Li, R.P. Gangloff, J.R. Scully, Hydrogen trap states in ultrahigh-strength aermet 100 steel, Metall. Mater. Trans. 35 (3) (2004) 849–864.
[44] S. Yamasaki, H. Bhadeshia, M4c3 precipitation in fe–c–mo–v steels and relationship to hydrogen trapping, Proc. Math. Phys. Eng. Sci. 462 (2072) (2006) 2315–2330.
[45] C. Ayas, V. Deshpande, N. Fleck, A fracture criterion for the notch strength of high strength steels in the presence of hydrogen, J. Mech. Phys. Solid. 63 (2014) 80–93.
[46] R.A. Oriani, The diffusion and trapping of hydrogen in steel, Acta Metall. 18 (1) (1970) 147–157.
[47] P. Sofronis, Y. Liang, N. Aravas, Hydrogen induced shear localization of the plastic flow in metals and alloys, Eur. J. Mech. Solid. 20 (6) (2001) 857–872.
[48] J. J. Gilman, Micromechanics of Flow in Solids.
[49] J. Hirth, B. Carnahan, Hydrogen adsorption at dislocations and cracks in fe, Acta Metall. 26 (12) (1978) 1795–1803.
[50] R.P. Gangloff, B.P. Somerday, Gaseous Hydrogen Embrittlement of Materials in Energy Technologies: Mechanisms, Modelling and Future Developments, Elsevier, 2012.
[51] H.K. Birnbaum, P. Sofronis, Hydrogen-enhanced localized plasticityâ€”a mechanism for hydrogen-related fracture, Mater. Sci. Eng., A 176 (1–2) (1994) 191–202.
[52] I. Robertson, The effect of hydrogen on dislocation dynamics, Eng. Fract. Mech. 68 (6) (2001) 671–692.
[53] Y. Liang, P. Sofronis, R. Dodds Jr., Interaction of hydrogen with crack-tip plasticity: effects of constraint on void growth, Mater. Sci. Eng., A 366 (2) (2004) 397–411.
[54] Y. Liang, P. Sofronis, N. Aravas, On the effect of hydrogen on plastic instabilities in metals, Acta Mater. 51 (9) (2003) 2717–2730.
[55] P. Sofronis, R.M. McMeeking, Numerical analysis of hydrogen transport near a blunting crack tip, J. Mech. Phys. Solid. 37 (3) (1989) 317–350.
[56] O. Nguyen, M. Ortiz, Coarse-graining and renormalization of atomistic binding relations and universal macroscopic cohesive behavior, J. Mech. Phys. Solid. 50 (8) (2002) 1727–1741.
[57] R.L. Hayes, M. Ortiz, E.A. Carter, Universal binding-energy relation for crystals that accounts for surface relaxation, Phys. Rev. B 69 (17) (2004) 172104.

[58] E. Hondros, M. Seah, The theory of grain boundary segregation in terms of surface adsorption analogues, Metallurgical Transactions A 8 (9) (1977) 1363–1371.
[59] L. Vergani, G. Gobbi, C. Colombo, A numerical model to study the hydrogen embrittlement effect on low-alloy steels, in: Key Engineering Materials, vol. 577, Trans Tech Publ, 2014, pp. 513–516.
[60] B. Healy, A. Gullerud, K. Koppenhoefer, A. Roy, S. RoyChowdhury, M. Walters, B. Bichon, K. ne Cochran, A. Carlyle, J. Sobotka, et al., Warp3d release 17.5.9): 3-d nonlinear finite element analysis of solids for fracture and fatigue processes, University of Illinois, Urbana-Champaign.doi:http://code.google.com/p/warp3d.
[61] C. Colombo, G. Fumagalli, F. Bolzoni, G. Gobbi, L. Vergani, Fatigue behavior of hydrogen pre-charged low alloy cr–mo steel, Int. J. Fatig. 83 (2016) 2–9.
[62] S. Roychowdhury, Y.D.A. Roy, R.H. Dodds Jr., Ductile tearing in thin aluminum panels: experiments and analyses using large-displacement, 3-d surface cohesive elements, Eng. Fract. Mech. 69 (8) (2002) 983–1002.
[63] K.-H. Schwalbe, A. Cornec, K. Baustian, Application of fracture mechanics principles to austenitic steels, Int. J. Pres. Ves. Pip. 65 (3) (1996) 193–207.